Photocatalytic degradation of benzene over different morphology BiPO₄: Revealing the significant contribution of high–energy facets and oxygen vacancies

Xiuzhen Zheng[a,1], Jinghui Wang[c,1], Jianjun Liu[b], Ziqun Wang[a], Shifu Chen[a], Xianliang Fu[a,*]

[a] College of Chemistry and Material Science, Huaibei Normal University, Huaibei, 235000, Anhui, China
[b] School of Physics and Electronic Information, Huaibei Normal University, Huaibei, 235000, Anhui, China
[c] Inner Mongolia Key Lab of Carbon Nanomaterials, Nano Innovation Institute(NII), College of Chemistry and Chemical Engineering, Inner Mongolia University for Nationalities (IMUN), Tongliao, 028000, China

ARTICLE INFO

ABSTRACT

Wide–band–gap BiPO₄ (BPO) is a promising candidate for photocatalytic degradation of highly stable benzene exhaust. To reveal the effect of the morphology and the oxygen vacancies of BPO on the degradation of benzene, a series of monoclinic BPO samples with the common reported rod– (BPO–R), sheet– (BPO–S), urchin– (BPO–U), and dendrite–like (BPO–D) morphology were synthesized and some oxygen vacancies were introduced in BPO–D. The samples were then used for photocatalytic degradation of gaseous benzene and the mineralization rate of benzene over the samples decreased in order BPO–D (258.6) > BPO–S (48.0) > BPO–U (21.0) > BPO–R (7.3 μmol h⁻¹ m⁻²). BPO–D with a dendritic morphology showed the highest activity. The highly energetic (002), (012), and (031) facets and the oxygen vacancies make great contributions to the high performance of BPO–D, which favor the absorption of BPO–D in long–wavelength range, the adsorption of reactants, the formation of O₂–· and eventually the interfacial degradation of benzene. The ESR and scavengers tests indicated that O₂–· and the photogenerated holes are the main active species responsible for the degradation of benzene. This work suggests that increasing the proportion of high–energy crystal facets and introduction of oxygen vacancies are effective strategies to improve the photocatalytic performance of BPO.

1. Introduction

TiO₂–based photocatalytic oxidation (PCO) processes have been regarded as a promising advanced oxidation technology for the remediation of environmental pollutants. [1] However, the application of TiO₂ for industrial purposes is still limited by its narrow absorption range and the quick recombination of photoinduced charger carriers (PCCs). Furthermore, when dealing with some specific pollutants, such as gaseous benzene, toluene, xylenes, and other aromatics, the activity of TiO₂ is very unsatisfactory. [2,3] A deactivation of TiO₂ occurs due to the deposition of stable by–products. To pursue a high PCO performance, many efforts have been devoted to the development of new photocatalytic materials to overcome these drawbacks, especially the visible–light photocatalysts [4–7]. Take for the degradation of benzene as example, some vanadates sensitized TiO₂ have been developed and showed stable activity for abatement of gaseous benzene. [8–11] However, in many cases, a high PCO performance cannot be guaranteed

by extending the absorption range of the photocatalyst because the redox capacity of the PCCs will be reduced with the narrowing of the band–gap energy, which results in a low mineralization efficiency of the pollutants. As artificial light sources can be used in PCO process, the redox capacity of PCCs is a priority in the degradation of pollutants rather than the absorption range. In this case, the degradation of the pollutants will be directly restricted by the redox capacity of the photogenerated holes (h⁺) and electrons (e–), as well as their separation efficiency. Therefore, development of wide–band–gap semiconductors also holds a great promise for the abatement of contaminants, especially for aromatic compounds that possess a very stable benzene ring.

Benzene, the prototype of the aromatic compounds, is a typical indoor volatile organic compound and has been regarded as a priority hazardous substance for its high carcinogenicity, toxicity, and environmental persistence [12]. However, benzene exhaust is still hard to be degraded by the traditional TiO₂, ZnO, and SnO₂ photocatalysts [13–17] for the deposition of refractory intermediates induced by h⁺

---

[18]. To suppress the formation of the by–products, some hydroxides such as In(OH)$_3$, InOOH, ZnSn(OH)$_6$, and GaOOH [17,19–22] were developed to strengthen the ·OH–mediated oxidation route. Another strategy for the abatement of benzene is to develop wide–band–gap photocatalysts such as Ga$_2$O$_3$, Sr$_2$Sb$_2$O$_7$, and Zn$_2$GeO$_4$ [15,23,24], which have sufficient redox capability to decompose the intermediates. As a typical wide–band–gap semiconductor, bismuth phosphate (BiPO$_4$, denoted as BPO) was firstly reported by Zhu's group to have excellent activity for the degradation of dyes and its performance was at least 2 times greater than the famous P25. [25–27] Thereafter, BPO–based photocatalysts were extensively documented in recent years. The photocatalytic application of BPO was mainly focused on the degradation of dyes [26–32] and phenols [29,30,33,34] effluents. However, the primary advantage of BPO, i.e. the stronger redox capacity of PCCs, has not been fully utilized in these applications because the decomposition of these pollutants also can be achieved successfully on the traditional TiO$_2$ and ZnO. It will be meaningful to use BPO for the degradation of highly stable benzene that is hard to be handled by traditional photocatalysts. Unfortunately, the PCO of benzene over BPO is still seldom. [35–37]

BPO can crystallize in hexagonal and monoclinic structures. The effect of the crystalline phase of BPO on the degradation of gaseous benzene was investigated in our recent work. [37] The result indicated that, rather than the hexagonal, the monoclinic phase of BPO is a preferred crystalline structure for the degradation of benzene due to the distortion of PO$_4$ tetrahedron and the largest band gap structure. Besides, the morphology of BPO and the oxygen vacancies in BPO have been reported to play some important roles in the degradation of dyes. [28,32,38–42] However, the effects of these factors on the degradation of benzene are still unrevealed. The investigation of these problems will be of great significance both for the development of highly active BPO photocatalysts and for the efficient remediation of benzene exhaust.

Herein, a series of monoclinic BPO samples with the common reported rod– [37,41], sheet– [43,44], urchin– [38,45,46], and dendrite–like [47] morphology were synthesized and some oxygen vacancies were introduced in the preparation of the dendritic BPO sample. Photocatalytic degradation of benzene over these BPO samples was then investigated and compared to reveal the key factors that dominate the degradation reaction. The main oxidative species responsible for the degradation of benzene were finally elucidated based on the ESR and the scavengers test results.

2. Experiments

2.1. Preparation of BPO samples

Bi(NO$_3$)$_3$·5H$_2$O, Na$_3$PO$_4$·12H$_2$O, HNO$_3$, H$_6$P$_4$O$_{13}$, and EDTA were of analytical grade and used as received from Aladdin Chemical Reagent Co. if not specified. Different morphology monoclinic phase of BPO samples were prepared by modified hydrothermal methods. [40,45–48] The resulted rod–, sheet–, urchin–, and dendrite– samples were denoted as BPO–R, BPO–S, BPO–U, and BPO–D, respectively.

For the preparation of BPO–R, 0.97 g Bi(NO$_3$)$_3$·5H$_2$O and 0.76 g Na$_3$PO$_4$·12H$_2$O were dissolved in 80 mL glycerol–water solution (volume ratio 1:2). The mixture was then transferred into an autoclave and kept in an oven at 200 °C for 3 h. For the preparation of BPO–S, 1.45 g Bi (NO$_3$)$_3$·5H$_2$O and 1.14 g Na$_3$PO$_4$·12H$_2$O were first dissolved in 30 mL H$_2$O. The solution pH was then adjusted to 1 by HNO$_3$ under vigorous stirring. The mixture was then transferred into an autoclave and kept in an oven at 180 °C for 72 h. BPO–U was prepared by a similar process to BPO–S except that the suspension was replaced by 2 g Bi (NO$_3$)$_3$·5H$_2$O + 40 mL of 0.3 M H$_6$P$_4$O$_{13}$. For the preparation of BPO–D, 0.97 g Bi(NO$_3$)$_3$·5H$_2$O, and 0.74 g EDTA were first added to 40 mL HNO$_3$ solution containing 275 µL 65% HNO$_3$. After the precursor was dissolved by oil bath heating, 0.76 g Na$_3$PO$_4$·12H$_2$O was added under vigorous stirring. The mixture was then hydrothermally treated at 180

°C for 24 h in an autoclave. The solid products formed after the hydrothermal treatments were collected by centrifugation, rinsed thoroughly with deionized water, and finally dried in an oven at 80 °C for 5 h.

2.2. Characterization

The crystal phase structures of the prepared BPO samples were determined by a Bruker D8 Advance X–Ray diffractometer (XRD, Cu Kα radiation, λ = 1.5406 Å). Raman spectra were acquired at room temperature in the range of 200–1500 cm^{-1} with a resolution of 1 cm^{-1} on a Raman microspectrometer (Renishaw inVia 2000, using an Ar ion laser, 514 nm). FTIR spectra of the BPO were recorded on a Thermo Nicolet Nexus 6700 FT–IR spectrophotometer by using KBr pellets in the range of 4000–400 cm^{-1}. The optical properties were analyzed by UV–vis diffuse reflectance spectra with BaSO$_4$ as a reference (UV–vis DRS, TU–1950, Persee) and photoluminescence emission spectra excited by 256 nm light at room temperature (PL, JASCO FP–8300). The morphology and structure of the samples were studied on a scanning electron microscope (SEM, Hitachi SU8000) and a transmission electron microscopy (TEM, JEOL JEM–2100 URP). Energy–dispersive analysis X–ray (EDAX) was carried out on an apparatus coupled to the SEM instrument. X–ray photoelectron spectroscopy (XPS) analysis was operated on a VG Escalab 250 photoelectron spectrometer with Al Kα X–ray beam (1486.6 eV). The binding energies were referred to the C 1 s peak at 284.6 eV. Multipoint Brunauer–Emmett–Teller specific surface areas (S$_{BET}$) of the BPO samples were determined from the BET transforming plot of the N$_2$ adsorption isotherms which were obtained at 77 K by using a Micromeritics ASAP 2020 surface area and porosity analyzer. Electron spin resonance (ESR) spectra of the prepared BPO samples were taken on a Bruker ESR 300 E ESR spectrometer at ca. 100 K in liquid N$_2$. To construct the band structure of the prepared BPO samples, the flat band positions (V$_{fb}$) of the samples were analyzed by the Mott–Schottky (M-S) plots on a CHI–660E electrochemical workstation (CHI instruments). The potential ranges from –1.0 to 0.2 V (vs Ag/AgCl) at a frequency of 500, 1000, and 1500 Hz. 0.2 M Na$_2$SO$_4$ aqueous solution was used as the electrolyte (the pH is ca. 7.0).

2.3. Photocatalytic degradation of gaseous benzene

Photocatalytic degradation of gaseous benzene was conducted in a quartz reactor in a continuous flow mode. Four UV lamps (254 nm, TUV 6 W/G6 T5) were assembled around the reactor as light source. A mixture of 0.2 g BPO and 2.0 g 50–70 mesh quartz sand (as support) was loaded on the reactor. The photocatalyst bed was then purged by benzene vapor (250 ppm, 30 mL/min, balanced by O$_2$) for 60 min in the darkness to establish adsorption−desorption equilibrium. After turning on the lamps, the residual benzene and the formed CO$_2$ were determined by an online gas chromatograph (Agilent 7820 A). The temperature of the photocatalyst bed was controlled at ca. 30 °C by a suction fan.

2.4. Determination of photoinduced active radicals

The formations of photoinduced ·OH and O$_2$·− on the BPO samples were measured by ESR technique under irradiation at room temperature on a Bruker ESR 300 E spectrometer with 5,5–dimethyl–1–pyrroline–N–oxide (DMPO, Sigma–Aldrich) as a spin–trap agent. Freshly–prepared suspension of 20 mg BPO in 0.5 mL DMPO (50 mM) aqueous or methanol solution was used for the measurement of ·OH and O$_2$·−, respectively. The ESR signals were measured every 30 s under illumination of 254 nm light.

2.5. Investigation the contributions of active species

Photoinduced h$^+$ and the derivatives of ·OH, and O$_2$·− commonly
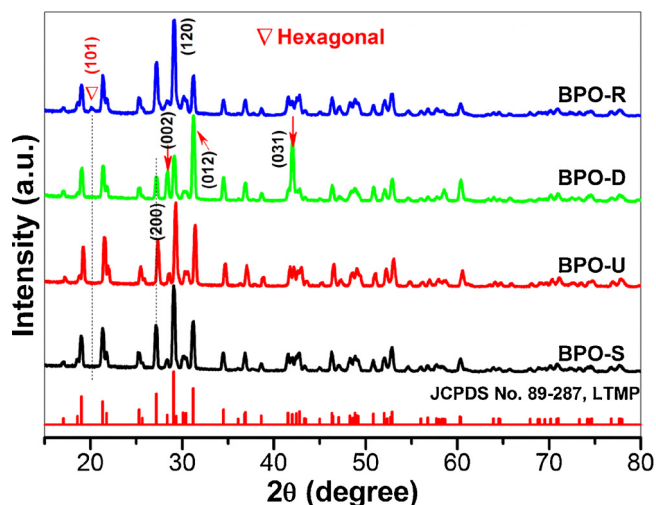
Fig. 1. XRD patterns of the prepared BPO samples. The bottom shows the standard XRD pattern of low–temperature monoclinic phase (LTMP) BiPO$_4$.

serve as active species for PCO process. To study the contribution of these species, some scavengers were introduced during the photocatalytic degradation of methyl orange solution (MO, chosen as a model reaction, 165 mL, 10 ppm) on 0.1 g BPO–D. The experimental procedure has been described in our previous works. [17,49] To evaluate the contribution of h$^+$ and ·OH, two tests were further performed in O$_2$ with 165 μL triethanolamine (TEOA) and tert–butyl alcohol (TAB) as h$^+$ [31,50,51] and ·OH [31,52,53] scavengers, respectively. To study the role of O$_2$·$^-$, two tests without use of scavengers were further performed in N$_2$ and O$_2$. The variation of MO concentration with irradiation time was monitored in these tests. The contribution of the active species then can be estimated according to the degradation efficiency.

3. Results and discussion

3.1. Characterization results

The crystal phase structure of the prepared BPO samples was investigated by XRD. As shown in Fig. 1a, the diffraction peaks of the samples can be indexed to the low–temperature monoclinic phase (LTMP) structure of BiPO$_4$ with a lattice parameter of a = 6.753, b = 6.943 and c = 6.475 Å (JCPDS No. 89–287, shown at the bottom of Fig. 1a). No peaks originated from other Bi species were detected except BPO–R, revealing the purity of the samples. As for BPO–R, a weak peak located at 20.1 ° can be further observed besides the peaks of LTMP BiPO$_4$, which can be ascribed to the (101) diffraction of hexagonal

BiPO$_4$. It suggests that BPO–R contains a trace amount of hexagonal phase BiPO$_4$. A further analysis discloses that the peaks' intensities of BPO–D at 2θ = 28.3, 31.2 and 41.6 degree (indicated by the red arrows) are significantly larger than those of the standard diffraction spectrum and the other BPO samples. These peaks can be assigned to the (002), (012), and (031) crystal planes of LTMP BPO. Taking (012) diffraction peak as an example, the relative strength ratio of R$_{(012)/(120)}$ in the standard pattern is only 0.66. However, for BPO–D, the value is as high as 2.07. The enhanced dominant of these diffraction peaks indicates that, unlike other BPO samples, the synthesized BPO–D is preferentially grown on (002), (012) and (031) planes. It should be caused by the addition of EDTA in the preparation of BPO–D. Zhang et al. [47] found that EDTA can serve as a complexing agent to control the release of Bi^{3+}, which benefits the development of a dendritic morphology structure. Furthermore, EDTA can act as a capping agent [47,48] and is preferentially adsorbed on certain crystal facets of BPO nucleus, enabling the retention of some highly energetic facets of (002) and (012). [47]

The structures of the prepared BPO samples were further investigated by Raman spectroscopy. As shown in Fig. 2a, the BPO samples show almost the same Raman spectra except the intensity. The spectra agree well with the reported LTMP BPO. [29,39,41] The bands at 232.7 and 279.9 cm^{-1} can be ascribed to the O–Bi–O stretching vibration, while other bands can be assigned to the vibrations of PO$_4$ group. [44,54,55] Specifically, the bands centered at 1034.7 and 966.5 cm^{-1} are ascribed to the asymmetric (ν_3) and symmetric (ν_1) stretching vibrations of P–O, whereas the bands at (403.5 and 458.8 cm^{-1}) and (553.2 and 595.5 cm^{-1}) correspond to the ν_2 and ν_4 bending vibration of the O–P–O in PO$_4$ units, respectively. EDTA has been used for the formation of BPO–D and it may remain in the product. However, the D–bands of C located at ca. 1360 cm^{-1} [34,56] cannot be observed in BPO–D Raman spectrum, excluding the presence of EDTA. The Raman bands intensity of BPO–D and BPO–R is substantially lower than that of BPO–U and BPO–S, which may be caused by the low crystallinity of the samples [29,55] or the containing of oxygen vacancies [41] which can decrease the symmetry of BPO.

Fig. 2b shows the FTIR spectra of the prepared BPO samples. Apparently, the spectra of the samples highly resemble each other in the range of 400–3000 cm^{-1}. The absorption bands located in the finger–print region and the functional group region are the vibration behaviors of tetragonal PO$_4$ and OH groups, respectively. Specifically, in the finger–print region, the band centered at 530 cm^{-1} can be assigned to ν_4(PO$_4$) [34,57–59], while the other three bands appearing at 553, 565, and 600 cm^{-1} (highlighted by the gray region in Fig. 2b) can be ascribed to the bending vibration of PO$_4$, i.e. δ(O–P–O) [54,60]. The band around 928 cm^{-1} corresponds to the symmetric stretching vibration of ν_1(PO$_4$). However, the ν_3 asymmetric stretching vibration of PO$_4$ splits
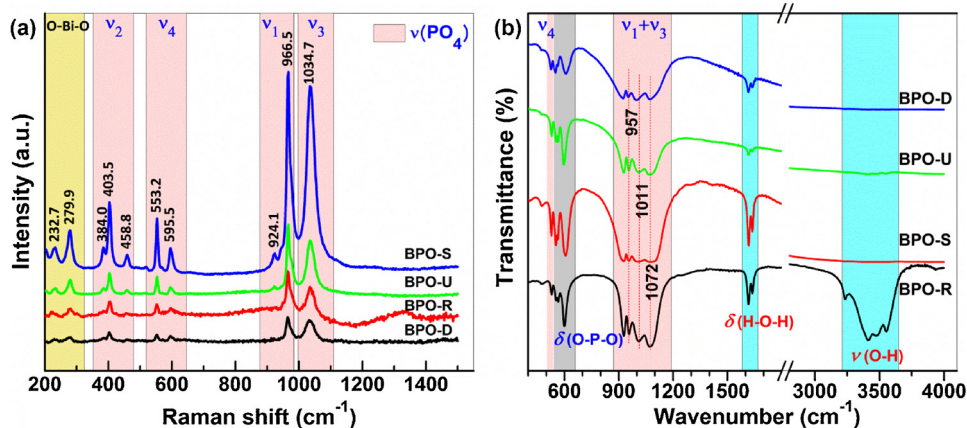

Fig. 2. (a) Raman and (b) FTIR spectra of the prepared BPO samples.

to three bands around 957, 1011, and 1072 cm^{-1}. [45,54,57,60,61] The splitting of these bands is the characteristic absorption of LTMP as the tetragonal PO$_4$ group is distorted in LTMP. [60,62] This result further confirms the formation of LTMP. In the functional group region, the absorption bands appeared at 1616 and 1637 cm^{-1} are the typical bending vibration δ(H–O–H) of water adsorbed on the samples surface. However, the corresponding stretching vibration ν(O–H) is very insignificant in BPO–D, BPO–U, and BPO–S and it can only be perceived in the magnified spectra (Fig. S1, the bottom right corner, see the electronic supporting information, ESI). But in BPO–R, the absorption bands of ν(O–H) are very intense. The band located at 3479 cm^{-1} can be ascribed to the water coordinated to Bi atoms, [40,54,57,58,62] while the band centered at 3552 cm^{-1} can be assigned to the water physically adsorbed on BPO surface. [57,58] This finding suggests that BPO–R contains of considerable lattice water that comes from the impurity phase of hexagonal BiPO$_4$ [54,58,62] that has been confirmed by XRD results (Fig. 1). The adsorption of water on BPO–R surface then can be boosted due to the hydrogen bonds interactions, which intensifies the ν(O–H) absorptions. The survival of EDTA in BPO–D is further excluded by the FTIR spectrum as the absorption bands of EDTA centered at 2855 and 2926 cm^{-1} [48] cannot be perceived in Fig. 2b, even in the magnified spectrum (Fig. S1, the top right corner).

The absorption properties of the synthesized BPO were characterized by UV–vis DRS. As shown in Fig. 3, some steep absorption around 300 nm can be observed, which can be attributed to the band–gap transition of BPO. The absorption thresholds (λ$_g$) decrease in order BPO–D (324) > BPO–S (315) > BPO–R (305) > BPO–U (290 nm). Obviously, BPO–D shows a broader absorption than other samples. In addition, as highlighted by the elliptical region in Fig. 3, a significant tail absorption in the long–wavelength region from 450 to 600 nm can be observed in BPO–D, which should be induced by the surface defects like the oxygen vacancies. [41,42,63] The defects lead to the change of BPO–D color from white to gray (see the inset of Fig. 3). A similar observation has been reported in Lv's works. [41,42] According to the equation of E$_g$ = 1240/λ$_g$, the band–gap energies (E$_g$) of BPO samples are estimated to be 3.8, 3.9, 4.1 and 4.3 eV for BPO–D, BPO–S, BPO–R and BPO–U, respectively, agreeing well with the reported values of 3.8–4.6 eV. [25,27] The Tauc plots [64] of (F(R) × hν)^n vs hν (eV) were further used to estimate the E$_g$ values, where F(R) is the absorption coefficient converted from R%, hν is the photon energy, and n equals 1/2 for indirect transition of BPO. [27,40] As shown in the inset of Fig. 3, the results are comparable to the values calculated by 1240/λ$_g$.

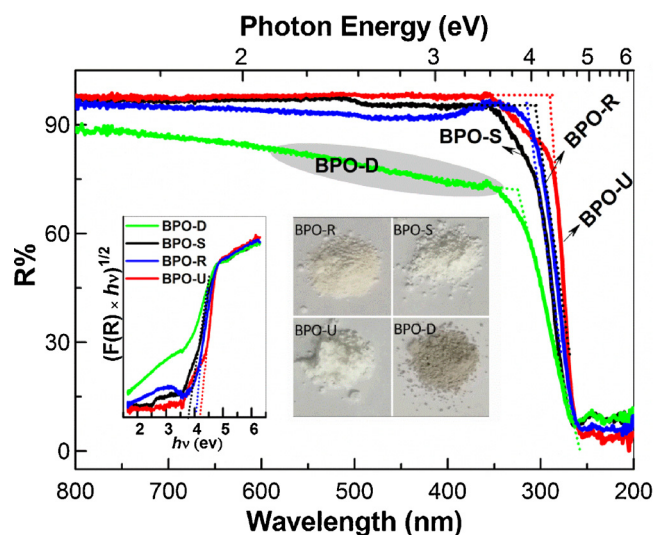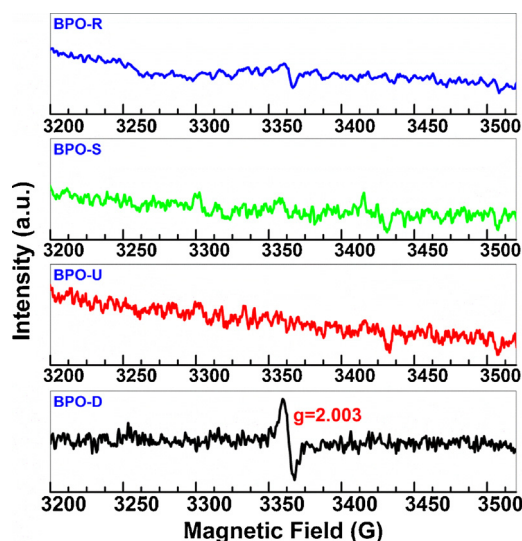The XRD results indicate that the prepared BPO samples are LTMP

Fig. 4. ESR spectra of the prepared BPO samples at ca. 100 K in liquid N$_2$.

BiPO$_4$. Therefore, rather than the phase structure, the discrepancy in the E$_g$ should be caused by other factors, such as the difference in morphology, the presence of oxygen vacancies, and the OH–related defects. [40,41] As shown in Fig. 3, the absorption of BPO–D is significantly different from other BPO samples and the difference should be caused by the use of EDTA. [47] The nucleation, crystallization, and the growth of BPO–D could be influenced by the chelation and the adsorption of EDTA in some BPO–D facets. [47,48] Consequently, the facets (002), (012), and (031) with high surface free energy can be retained as shown in Fig. 1 and some oxygen vacancies were introduced. The preferential growth of BPO–D nanostructure and the introduction of oxygen vacancies can narrow its band–gap energy and lead to the sub–absorption in the visible light region in Fig. 3.

ESR is a very sensitive technique to directly monitor the presence of singly charged oxygen vacancies with unpaired electrons. To confirm the formation of oxygen vacancies in BPO–D, the ESR spectra of the prepared BPO samples were measured at ca. 100 K in liquid N$_2$. As shown in Fig. 4, only BPO–D presents an obvious ESR signal at g = 2.003 (calculated by g = hν/βH), which can be attributed to an electron trapped on the surface oxygen vacancy. [41,63,65–67] The ESR result clearly confirms the formation of oxygen vacancies in BPO–D.

PL emission is resulting from the recombination of photogenerated e– and h$^+$ and the emission intensity is proportional to their recombination rate. To study the separation efficiency of photogenerated charge carriers, the synthesized BPO samples were then characterized by PL emission spectra. As shown in Fig. S2, under the excitation of 256 nm, an emission peak around 290 nm can be observed. A similar emission peak has been reported [55] and it can be attributed to the band–gap recombination of BPO. The intensity of the peaks decreases in order BPO–U > BPO–R > BPO–S > BPO–D. The emission signal of BPO–D is substantially lower than other samples, suggesting a low recombination rate of e– and h$^+$ on BPO–D. The recombination of e– and h$^+$ on BPO–D should be suppressed by the oxygen vacancies and the exposure of highly energetic facets. This will be discussed below.

Fig. 5 shows the SEM and TEM images of the synthesized BPO samples. From Fig. 5a, b, it can be found that BPO–R is mainly composed of some rod–like particles with a length of ca. 700 nm and a width of 100 nm. The rods surface is covered by some fine particles with no specific morphology. The rod–shaped BPO should grow through the Ostwald ripening mechanism [40,54,59,61] and the small grains are the residuals of the primary particles after the maturation of BPO nanorods. To confirm the Ostwald ripening process, the tip of the rod was further characterized by HRTEM. As shown in Fig. 5b–1, two
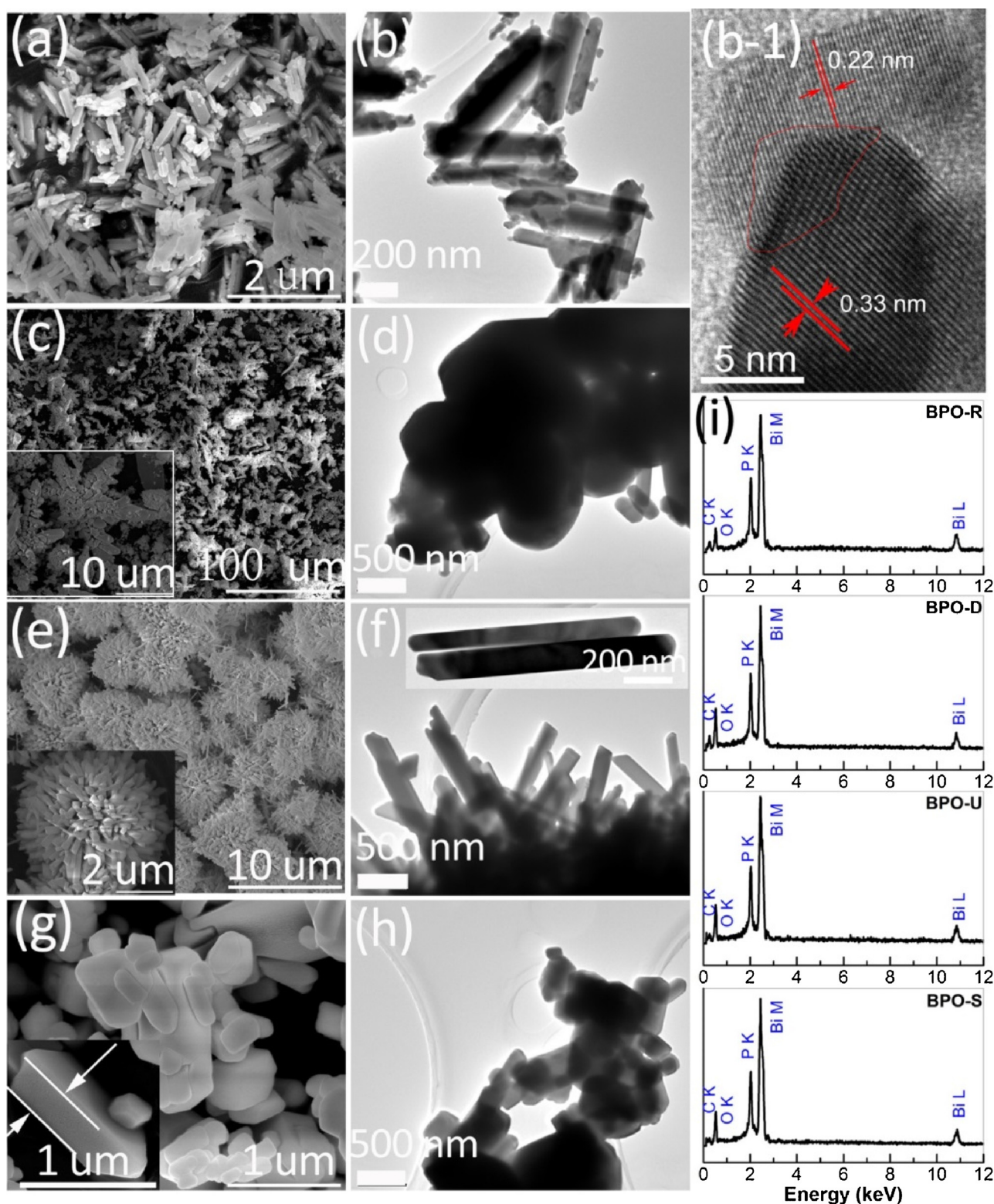

Fig. 3. UV–vis DRS patterns of the prepared BPO samples. Inset shows the corresponding Tauc plots and the pictures of the samples.

Fig. 5. SEM and TEM/HRTEM images of the prepared BPO samples: (a, b, b–1) BPO–R, (c, d) BPO–D, (e, f) BPO–U, and (g, h) BPO–S. (i) EDAX spectra of the BPO samples.

sets of lattice fringes with d values of 0.33 and 0.22 nm can be ob-served, which originate from the tip of the rod and the adhered particle, respectively. The lattice fringes can be attributed to the interplanar spacing of the (200) and (031) facets of LMTP BiPO₄. As indicated in the red circle region in Fig. 5b–1, the lattice fringes were fused around the contact interface between the rod and the grain, suggesting that the

rods grow epitaxially through absorbing small nano–particles via the Ostwald ripening mechanism. This growth process results in the con-version of (031) to a relatively stable (200) crystal plane. Fig. 5c and d indicate that BPO–D has a dendritic morphology and the branching size is ca. 20 μm (as shown in the inset of Fig. 5c). The addition of EDTA leads to the formation of this morphological structure [47]. Fig. 5e and f
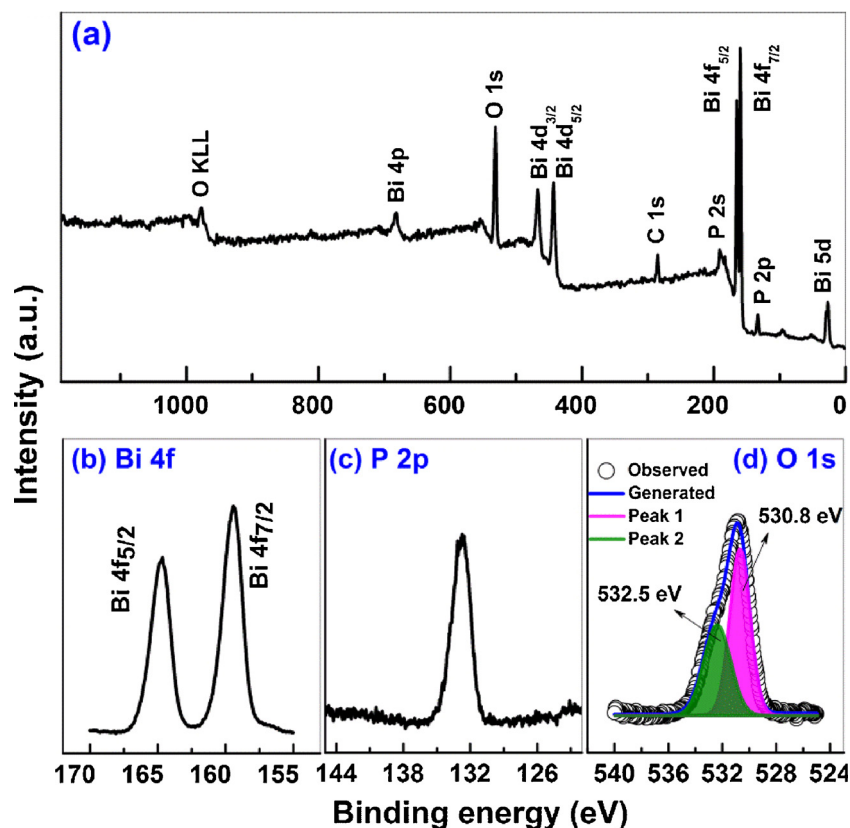
Fig. 6. (a) survey and high resolution XPS spectra of (b) Bi 4f, (c) P 2p, and (d) O 1s of the prepared BPO–D.

show that the BPO–U consists of uniformly dispersed architectures with a size of ca. 5 μm, which are closely packed by nanorods that extend radially from the same core (as shown in the inset of Fig. 5e). The diameter and length of the rods are ca. 100 nm and 1 μm, respectively (Fig. 5f). As shown in Fig. 5g and h, BPO–S has a flaky morphology. The sheets 2D sizes are within 1 μm, and the slice thickness is ca. 200 nm. The surface of the sheets is quite smooth. The compositions of the synthesized BPO samples were analyzed by EDAX. The spectra (Fig. 5i) reveal that the constituent of the BPO samples is Bi, O, and P and the atomic ratios are summarized in the Tab. 1. Apparently, the atomic ratios of Bi:O:P are comparable to the theoretical value of 1:1:4.

The composition and the valence state of the elements on the synthesized BPO samples were analyzed with BPO–D as the representative. The survey spectrum (Fig. 6a) indicates that the constituent of BPO–D is Bi, O, and P, except for the adventitious C. High resolution XPS spectra of Bi 4f, P 2p, and O 1 s were analyzed. The peaks of Bi $4f_{7/2}$ and $4f_{5/2}$ located at the binding energy of 159.5 and 164.7 eV can be found in Fig. 6b, which agree well with the binding energy of the Bi^{3+} state in $BiPO_4$. [34,68] P 2p peak locates at 132.7 eV (Fig. 6c) and it can be assigned to a +5 oxidation state P [32]. A broaden asymmetric O 1 s can be resolved in Fig. 6d. The peak can be further deconvoluted into two peaks centred at 532.5 (Peak 1) and 530.8 eV (Peak 2), respectively, suggesting the existence of two kinds of oxygen species on BPO–D surface. Peak 1 can be assigned to the surface–adsorbed O species, such as –OH and –OO arising from the adsorbed H_2O and O_2, while Peak 2 can be attributed to the lattice O in $BiPO_4$. [32,68,69] The content of the adsorbed O species is estimated to be 38% based on Peak 1 and 2 areas. Similar results also can be observed on BPO–R with an adsorbed O content of 44% (Fig. S3). The adsorbed O contents on these BPO samples are comparable to the reported result [68]. These findings suggest that H_2O and O_2 can be easily adsorbed on BPO, which can facilitate the PCO process as H_2O and O_2 are the precursors of the active

species.

3.2. Photocatalytic degradation of gaseous benzene

Benzene is a common indoor volatile organic pollutant and it is still hard to be degraded by commonly used TiO_2, ZnO, and SnO_2. [13–1721] BPO is a typical wide–band–gap semiconductor. Theoretically, the PCCs formed on BPO have a strong redox power to crack and mineralize the benzene ring. However, degradation of aromatic compounds on BPO is still seldom [35–37]. For the consideration, the PCO of gaseous benzene on the prepared BPO samples was investigated. Control tests indicated that benzene cannot be degraded without of BPO or irradiation. The degradation of benzene only can be reached when BPO and the irradiation were both satisfied. Fig. 7 shows the changes of the residual benzene and the degradation product CO_2 with illumination time. The initial concentration of benzene vapor is ca. 250 ppm and no CO_2 can be detected. After turning on the lights, benzene concentration decreases immediately, while CO_2 concentration increases rapidly. Steady reaction states can be reached after irradiation for about 100 min. The residual benzene and the generated CO_2 concentrations at steady state were (159.7, 322.5 ppm), (8.5, 1042.6 ppm), (63.2, 774.8 ppm), and (42.2, 860.5 ppm) for BPO–R, BPO–D, BPO–U, and BPO–S, respectively. BPO–D shows the highest degradation activity and the residual benzene is only 8.5 ppm and the generated CO_2 concentration is as high as 1042.6 ppm.

To compare the PCO efficiency of the prepared BPO samples, the conversion (C%) and the mineralization efficiencies (M%) of benzene were calculated by Eqs. 1 and 2 according to the steady–state reaction data, respectively.

$$C\% = \frac{[C_6H_6]_{initial} - [C_6H_6]_{steady}}{[C_6H_6]_{initial}} \times 100\%$$
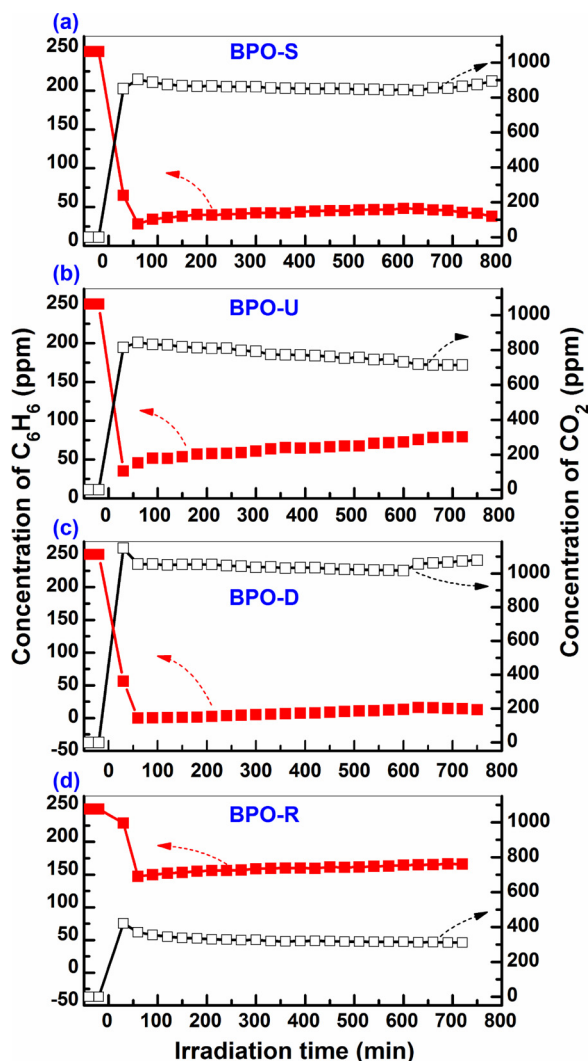
(1)

Fig. 7. The variation of residual C_6H_6 and generated CO_2 as a function of irradiation time over the prepared BPO samples.

$$M\% = \frac{[CO_2]_{steady}}{([C_6H_6]_{initial} - [C_6H_6]_{steady}) \times 6} \times 100\% \qquad (2)$$

As shown in Fig. 8, the C% of benzene on the BPO samples decreases in order of BPO–D (96.6%) > BPO–S (83.1%) > BPO–U (74.7%) > BPO–R (36.1%). BPO–R shows the lowest conversion efficiency, while BPO–D shows the highest conversion efficiency (as high as 96.6%). The M% of benzene (based on the converted benzene) decreases in order of BPO–D (72.0%) > BPO–S (69.0%) ≈ BPO–U (69.1%) > BPO–R (59.5%). BPO–R shows the lowest mineralization efficiency of benzene, while the other samples have a comparable mineralization efficiency of ca. 70%. Apparently, BPO–D shows the highest benzene degradation efficiency than other BPO samples.

The stability of BPO-D was tested by a 4-round cycle experiment. As shown in Fig. S4, in the four cycle experiments, the steady state benzene and CO_2 concentrations were maintained at ca. 10 and 1040 ppm, respectively, and no deactivation of the sample was observed. The spent BPO-D shows almost the same XRD pattern and the gray color (Fig. S5) as that of the fresh one confirming the stability of the high–energy crystal facets and the oxygen vacancies that causes the sample to change from white to gray. Thus, the stability of BPO-D can be largely approved by these results.

Fig. S6 shows the N_2 adsorption–desorption isotherms of the prepared BPO samples. The BET surface areas were measured and
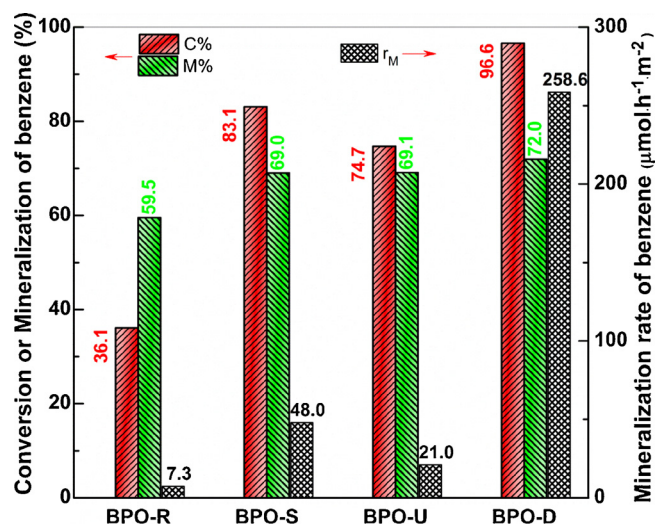

Fig. 8. Comparison the conversion, mineralization and mineralization rate of C_6H_6 achieved on the prepared BPO samples.

summarized in Table 1. Based on the steady CO_2 concentrations and the BET surface areas of the BPO samples, the complete mineralization rates (r_m, μmol·h^{-1} m^{-2}) of benzene into CO_2 were calculated by Eq. 3 with the feed gas treated as an ideal gas.

$$r_M = \frac{[C_6H_6]_{initial} \times 30(mL/min) \times 60(min) \times C\% \times M\%}{22.4(L/mol) \times 0.2(g) \times S_{BET}(m^2/g)} \qquad (3)$$

The r_M results are more intuitive and accurate than the conversion and mineralization efficiencies to reflect the real degradation of benzene as the calculation is based on the final decomposition product of CO_2. As shown in Fig. 8, the mineralization rate of benzene on the prepared BPO is significantly different and decreases in order BPO–D (258.6) > BPO–S (48.0) > BPO–U (21.0) > BPO–R. (7.3 μmol h^{-1} m^{-2}). BPO–D with a dendritic morphology shows the highest mineralization rate, which is more than 5 times higher than other samples. Although the rods–like BPO–R shows the largest BET surface area (2.90 m^2/g), the low conversion and mineralization efficiencies result in the lowest mineralization rate of benzene, only 7.3 μmol h^{-1} m^{-2}. Obviously, the dendritic BPO–D is more conducive to the degradation of benzene, followed by the sheet–like structure BPO–S and the urchin–like BPO–U. Here, it should be pointed out that the prepared BPO samples have a significantly higher activity than the well–known P25 photocatalyst. The mineralization rate of benzene on P25 is only 0.34 μmol h^{-1} m^{-2} and a deactivation of P25 is observed with reaction prolonged due to the deposition of stable intermediates. [17,49,70].

BPO–S, BPO–U, and BPO–R show almost the same crystalline and exposed facets structures and no oxygen vacancies were introduced. Among them, the highest activity of BPO–S should be attributed to its relatively narrow band gap energy, [28] while the lowest performance of BPO–R should be caused by the impurity phase of hexagonal BPO that has been confirmed to be unfavorable for the degradation of benzene [37].

Compared with other BPO samples, BPO–D shows much higher activity for the degradation of gaseous benzene. The high performance can be attributed to the following two aspects: First, the unique dendritic morphological structure and the oriented growth of the crystal planes enable BPO–D to expose more highly active facets, especially the (002) plane. The surface energies of the typical BPO planes have been investigated by Zhang et al. [47] and the results indicated that (002) facet has the largest surface energy because a lot of Bi and O atoms are exposed. Our calculation results about the facets of (002), (200), (012), and (031) also confirm this truth (See the section of "Calculation the surface free energy of BPO" in the ESI). The surface energies of (002)

Table 1
Summarize the preparation, characterization, and photocatalytic activity results of the prepared BPO samples.

Sample	Phase	E_{cb} (v)[a]	E_{vb} (v)[a]	E_g (eV)	S_{BET} (m^2/g)	Content (At.%)			Degradation of C$_6$H$_6$		
						Bi	P	O	C%	M%	r_M[b]
BPO–R	LTMP	−0.51	3.52	4.03	2.90	17.0	18.5	64.5	36.0	59.6	7.33
BPO–S	LTMP	−0.70	3.22	3.92	1.20	17.0	18.4	64.6	83.1	69.0	48.0
BPO–U	LTMP	−0.69	3.55	4.24	2.47	16.6	17.3	66.0	74.7	69.1	21.0
BPO–D	LTMP	−0.65	3.17	3.82	0.27	15.7	16.7	67.6	96.6	72.0	258.6

[a] *vs.* NHE, at pH 7.
[b] μmol h^{-1} m^{-2}.

and (012) are as high as 2.59 and 2.14 J/m^2, respectively, which are more than 3 times higher than that of the predominant (200) facet (only 0.67 J/m^2) in the standard BPO JCPD card. More unsaturated atoms can be expected on these highly energetic facets [47] and they can serve as trap sites for the absorption of O$_2$, H$_2$O, and benzene and consequently facilitate the redox reaction induced by PCCs. The recombination of charge carriers then can be suppressed. Thus, a BPO sample with a large proportion of (002) facets can show high photocatalytic performance as observed in the degradation of methylene blue. [47] As indicated by Fig. 1, the percentage (002) facet of BPO–D is much larger than other BPO samples. Besides, the proportions of other crystal planes (012) and (031) with high surface energy in BPO–D are also significantly larger than other BPO samples. We believe that these facets have a similar facilitation to the PCO process as that of (002) planes. This is the first reason for the high activity of BPO–D. As we known, the significant contribution of these highly energetic facets of BPO to BPO photocatalytic performance has not been revealed in previous studies. Second, the presence of oxygen vacancies also partially accounts for the high PCO performance of BPO–D. The oxygen vacancies have dual beneficial effects on the PCO efficiency. According to Lv's work, [42] a broadening of the valence band width can be induced by the oxygen–vacancy states, which leads to the rise of valence band maximum and consequently the narrowing of band gap energy. This change has been confirmed in Fig. 3 as the photoresponse of BPO–D was extended to the visible light region and the absorption coefficient also was enhanced. Besides, oxygen vacancies can serve as trap sites for PCCs [41,42] and adsorption sites for O$_2$ [71,72]. The reduction of O$_2$ to O$_2$–· by photoinduced e– than can be promoted, as well as the separation of PCCs. The low recombination of PCCs and the high formation efficiency of O$_2$–· have been verified by the PL (Fig. S2) and ESR (Fig. 9, see below) results, respectively.

In summary, the high PCO performance of BPO–D can be attributed to its high proportion of (002), (012), and (031) facets with high–surface–energy and the presence of oxygen vacancies. These facets and the oxygen vacancies make significant contributions to the PCO of benzene.

3.3. Degradation mechanism

O$_2$–·, ·OH and holes are the main active species in the photocatalytic degradation process. Among them, O$_2$–· and ·OH can be detected by ESR technique with DMPO as a trapping agent. To study the photocatalytic degradation mechanism of benzene on BPO, the photoinduced O$_2$–· and ·OH was investigated with BPO–D and BPO–R as the representatives. Fig. 9 shows the ESR spectra of the DMPO–O$_2$–· and –·OH adducts formed over BPO–D with irradiation time. As shown in Fig. 9a, the sextet characteristic peaks of DMPO–O$_2$–· [73,74] can be observed immediately after turning on the lamp and the peaks intensity increases gradually with irradiation time. Meanwhile, the four–fold characteristic peak of DMPO–·OH adducts with an intensity ratio of 1:2:2:1 can be found in Fig. 9b [21,75]. However, the peaks' intensity of DMPO–·OH is significantly lower than that of DMPO–O$_2$–· and is not improved with time. The result suggests that, compared to O$_2$–·, ·OH

cannot be effectively produced on BPO–D.

Theoretically, the generation of ·OH is proportional to the photocatalyst surface –OH concentration. A surface with a high density of –OH groups can promote the formation of ·OH. The FTIR result (Fig. 2b) indicates that the surface of BPO–R is rich in –OH group. However, the ESR analysis results of BPO–R (Fig. S7) are highly similar to those of BPO–D. The peaks of DMPO–O$_2$–· are more pronounced than that of DMPO–·OH and the intensity of DMPO–·OH signal also showed no apparent improvement with illumination time. Thus, it can be concluded that O$_2$–· is the predominant active species on BPO rather than ·OH. The low formation efficiency of ·OH is not determined whether the BPO surface is rich in hydroxyl group.

In our previous study of ZnSn(OH)$_6$ photocatalyst [17,70], it was found that the ESR signal of DMPO–·OH is significantly stronger than that of DMPO–O$_2$–· and the PCO of benzene was dominated by ·OH–mediated degradation process. The opposite results observed here on BPO samples suggest that ·OH radicals derived from photogenerated h$^+$ do not dominate the degradation of benzene. Photoinduced h$^+$ may directly participate in the oxidation of benzene on BPO. To reveal the contribution of O$_2$–·, ·OH, and h$^+$ in the PCO process, a series of comparative experiments were conducted in the presence of different active species scavengers with the decolorization of MO solution as a probe reaction. The reason for choosing the degradation of MO as a model reaction has been clarified in the ESI.

O$_2$–· is generated from the reduction of adsorbed O$_2$ by photoinduced e– and has been confirmed by ESR spectroscopy. To demonstrate the contribution of O$_2$–·, the decoloration of MO was first examined by purging with N$_2$ and O$_2$ (20 mL/min), respectively. [33] As shown in Fig. S8–a, b and Fig. 10, the decolorization of MO is dramatically reduced under N$_2$ atmosphere as e—derived O$_2$–· cannot be generated in this case, even the reaction is performed without the addition of ·OH and h$^+$ trapping agents. Thus, one of the critical active species responsible for the high PCO performance of BPO is O$_2$–·. The photoinduced h$^+$ can involve in the PCO process directly through itself or indirectly through the derivative ·OH radicals. To reveal which one predominates the high PCO efficiency of BPO, another two tests for the decolorization of MO under O$_2$ atmosphere were performed with TEOA and TBA as h$^+$ and ·OH scavengers, respectively [31,50–53]. As shown in Fig. S8–c, d and Fig. 10, compared to the reaction without any scavengers, the decolorization efficiencies of MO in the tests are reduced, especially for TEOA–added test. That means the decolorization of MO was greatly retarded when photoinduced h$^+$ was scavenged by TEOA. However, for the test performed in TBA–added solution, although ·OH radicals were trapped by TBA, the degradation of MO is only slightly reduced. This result suggests that the photoinduced h$^+$ on BPO can directly involve in the PCO process and make a greater contribution to the high activity of BPO than ·OH radicals. The photogenerated h$^+$ on BPO has strong oxidation power. Liu's work [76] indicated that, in the degradation of phenols, the aromatic intermediates cannot be mineralized by ·OH radicals, but can be done efficiently by h$^+$. Thus, the direct reaction of h$^+$ with benzene is essential for the cleavage of benzene ring, which provides a crucial premise for the subsequent mineralization triggered by O$_2$–·.
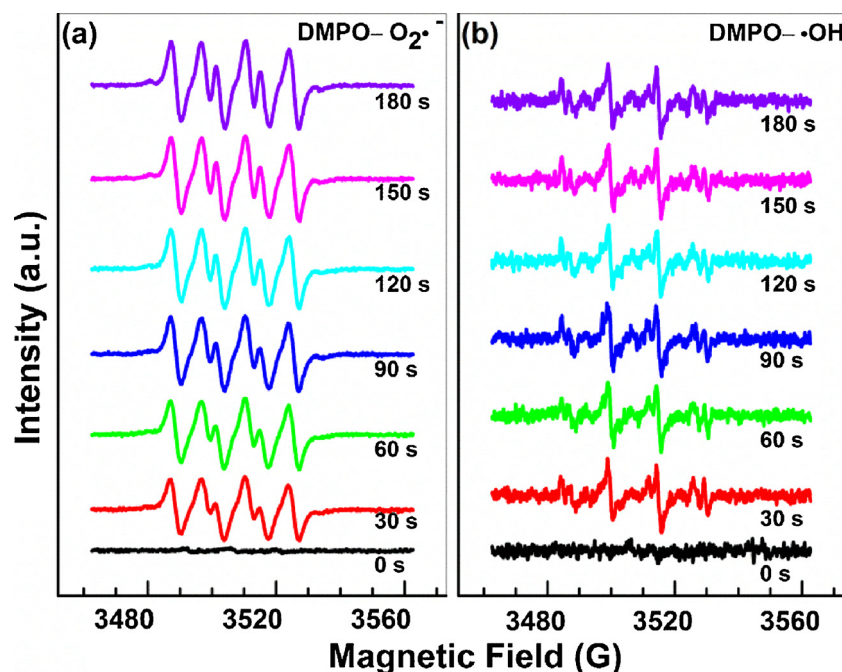
Fig. 9. ESR spectra of (a) DMPO–O$_2$$^·$– and (b) DMPO–$^·$OH adducts formed with irradiation time (254 nm light) in the suspension of BPO–D.
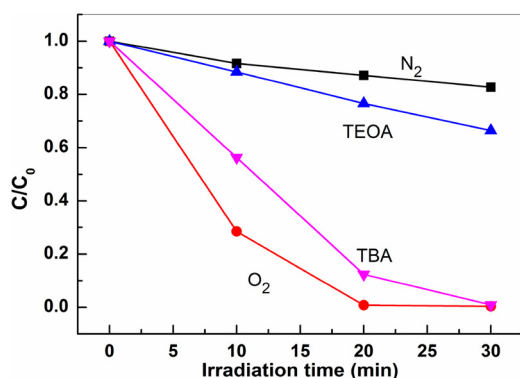

Fig. 10. Photocatalytic decolorization of MO on BPO–D under different reaction atmosphere or with the addition of different scavengers.

M-S plots have been used to construct the band structure of the BPO samples. As shown in Fig. S9, the plots indicated that the V_{fb} of BPO-R, BPO-S, BPO-U, and BPO-D are -0.41, −0.60, -0.59, and −0.55 V (*vs.* Ag/AgCl), respectively. Considering the similarity in composition and the feature of insulating n-type semiconductor, the difference between E_{fb} and the bottom of conduction band (E_{cb}) of the samples was assumed to be 0.3 V. [25,37,77] Therefore, the E_{cb} of BPO-R, BPO-S, BPO-U, and BPO-D are ca. −0.51, -0.7, −0.69, and −0.65 V (*vs.* NHE, at pH 7), respectively. The corresponding valence band edge (E_{vb}) then can estimate to be 3.52, 3.22, 3.55, and 3.17 V. Obviously, the photogenerated h$^+$ on the BPO samples have high oxidation potential to cleavage of benzene ring.

Therefore, both the ESR and scavengers tests suggest that O$_2$–$^·$ and the photogenerated h$^+$ are the main active species of BPO, agreeing well with the reported works. [33,39,42,76] We think that this collusion is fully applicable to the degradation of gaseous benzene because the reaction was performed under a vapor–scarce atmosphere and the formation of ·OH radicals will be unfavored due to the deficiency of water. Photogenerated h$^+$ will react more easily with benzene than liquid solid phase reaction systems.

Based on the characterization and the degradation results obtained on the different morphology BPO samples, the degradation process of benzene on BPO–D can be briefly described in Fig. 11. Charge carriers are first generated in BPO bulk under activation. Subsequently, these charge carriers migrate to BPO surface and then involve in the interfacial reactions. The separation of charge carriers can be accelerated by the exposure of high–energy facets of (002), (012), (031) and the presence of oxygen vacancies as they can enhance the adsorption of reaction substrates (such as O$_2$, H$_2$O and benzene) and promote the formation of O$_2$–$^·$ and the direct reaction of h$^+$ with benzene. Photoinduced h$^+$ and O$_2$–$^·$ are the main active species responsible for
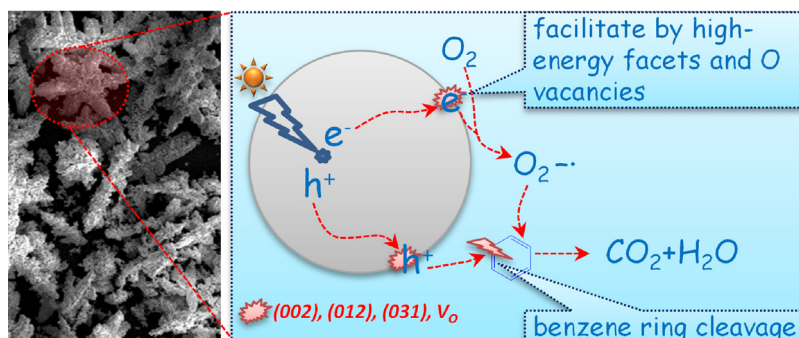

Fig. 11. Illustration the photocatalytic degradation process of benzene over BPO–D under UV light irradiation.

the degradation of benzene. The direct reaction of highly active h$^+$ with benzene leads to the cleavage of benzene ring, a crucial step for the mineralization of benzene triggered by O$_2$–$^{\cdot}$.

4. Conclusions

A series of monoclinic BPO samples with the commonly reported rod–, sheet–, urchin–, and dendrite–like morphology were synthesized and used for photocatalytic degradation of gaseous benzene. The mineralization rates of benzene over the samples decreases in order BPO–D (258.6) > BPO–S (48.0) > BPO–U (21.0) > BPO–R (7.3 µmol h^{-1} m^{-2}). BPO–D with a dendritic morphology shows the highest performance, which can be attributed to its high proportion of (002), (012), and (031) facets with high surface energy and the presence of surface oxygen vacancies. These features favor the absorption of BPO–D in long–wavelength range, the adsorption of reactants, the formation of O$_2$–$^{\cdot}$ and finally the interfacial degradation of benzene. The ESR and scavengers tests indicate that O$_2$–$^{\cdot}$ and the photogenerated h$^+$ are the main active species responsible for the degradation of benzene.

Acknowledgements

Appendix A. Supplementary data

Supplementary material related to this article can be found, in the online version, at doi:https://doi.org/10.1016/j.apcatb.2018.11.029.

References

[1] M.R. Hoffmann, S.T. Martin, W.Y. Choi, D.W. Bahnemann, Chem. Rev. 95 (1995) 69–96.
[2] Y. Luo, D.F. Ollis, J. Catal. 163 (1996) 1–11.
[3] H. Einaga, S. Futamura, T. Ibusuki, Appl. Catal. B Environ. 38 (2002) 215–225.
[4] R. Asahi, T. Morikawa, T. Ohwaki, K. Aoki, Y. Taga, Science 293 (2001) 269–271.
[5] C. Zhang, Y.F. Zhu, Chem. Mater. 17 (2005) 3537–3545.
[6] X. Wang, K. Maeda, A. Thomas, K. Takanabe, G. Xin, J.M. Carlsson, K. Domen, M. Antonietti, Nat. Mater. 8 (2009) 76–80.
[7] M. Pelaez, N.T. Nolan, S.C. Pillai, M.K. Seery, P. Falaras, A.G. Kontos, P.S.M. Dunlop, J.W.J. Hamilton, J.A. Byrne, K. O'Shea, M.H. Entezari, D.D. Dionysiou, Appl. Catal. B Environ. 125 (2012) 331–349.
[8] J.X. Wang, H. Ruan, W.J. Li, D.Z. Li, Y. Hu, J. Chen, Y. Shao, Y. Zheng, J. Phys. Chem. C 116 (2012) 13935–13943.
[9] H. Huang, D. Li, Q. Lin, W. Zhang, Y. Shao, Y. Chen, M. Sun, X. Fu, Environ. Sci. Technol. 43 (2009) 4164–4168.
[10] G. Xiao, X. Wang, D. Li, X. Fu, J. Photochem. Photobiol. A Chem. 193 (2008) 213–221.
[11] Y. Hu, D. Li, Y. Zheng, W. Chen, Y. He, Y. Shao, X. Fu, G. Xiao, Appl. Catal. B Environ. 104 (2011) 30–36.
[12] US Environmental Protection Agency, US Government Printing Office: Washington, DC, 1996; Chapter 1, Part 423, App A.
[13] J. Du, W. Chen, C. Zhang, Y. Liu, C. Zhao, Y. Dai, Chem. Eng. J. 170 (2011) 53–58.
[14] H. Einaga, S. Futamura, T. Ibusuki, Phys. Chem. Chem. Phys. 1 (1999) 4903–4908.
[15] J. Huang, X. Wang, Y. Hou, X. Chen, L. Wu, X. Fu, Environ. Sci. Technol. 42 (2008) 7387–7391.
[16] F. He, J. Li, T. Li, G. Li, Chem. Eng. J. 237 (2014) 312–321.
[17] X. Fu, J. Wang, D. Huang, S. Meng, Z. Zhang, L. Li, T. Miao, S. Chen, ACS Catal. 6 (2016) 957–968.
[18] O. D'Hennezel, P. Pichat, D.F. Ollis, J. Photochem. Photobiol. A Chem. 118 (1998) 197–204.
[19] T. Yan, J. Long, X. Shi, D. Wang, Z. Li, X. Wang, Environ. Sci. Technol. 44 (2010) 1380–1385.
[20] Z.H. Li, Z.P. Xie, Y.F. Zhang, L. Wu, X.X. Wang, X.Z. Fu, J. Phys. Chem. C 111 (2007) 18348–18352.
[21] X. Fu, X. Wang, Z. Ding, D.Y.C. Leung, Z. Zhang, J. Long, W. Zhang, Z. Li, X. Fu, Appl. Catal. B Environ. 91 (2009) 67–72.
[22] M. Sun, D. Li, W. Zhang, X. Fu, Y. Shao, W. Li, G. Xiao, Y. He, Nanotechnology 21 (2010) 355601.
[23] Y. Hou, L. Wu, X. Wang, Z. Ding, Z. Li, X. Fu, J. Catal. 250 (2007) 12–18.
[24] H. Xue, Z. Li, L. Wu, Z. Ding, X. Wang, X. Fu, J. Phys. Chem. C 112 (2008)
[25] C. Pan, D. Li, X. Ma, Y. Chen, Y. Zhu, Catal. Sci. Technol. 1 (2011) 1399–1405.
[26] C. Pan, Y. Zhu, J. Mater. Chem. 21 (2011) 4235–4241.
[27] C. Pan, Y. Zhu, Environ. Sci. Technol. 44 (2010) 5570–5574.
[28] G. Li, Y. Ding, Y. Zhang, Z. Lu, H. Sun, R. Chen, J. Colloid Interf. Sci. 363 (2011) 497–503.
[29] Y.F. Liu, Y.H. Lv, Y.Y. Zhu, D. Liu, R.L. Zong, Y.F. Zhu, Appl. Catal. B-Environ. 147 (2014) 851–857.
[30] Z. Zhang, H. Liu, J. Xu, H. Zeng, J. Photochem. Photobiol. A Chem. 336 (2017) 25–31.
[31] Y. Liu, P. Zhang, H. Lv, J. Guang, S. Li, J. Jiang, RSC Adv. 5 (2015) 83764–83772.
[32] H. Lv, J. Guang, Y. Liu, H. Tang, P. Zhang, Y. Lu, J. Wang, RSC Adv. 5 (2015) 100625–100632.
[33] Y. Liu, W. Yao, D. Liu, R. Zong, M. Zhang, X. Ma, Y. Zhu, Appl. Catal. B Environ. 163 (2015) 547–553.
[34] J. Di, J. Chen, M. Ji, Q. Zhang, L. Xu, J. Xia, H. Li, Chem. Eng. J. 313 (2017) 1477–1485.
[35] B. Long, J. Huang, X. Wang, Prog. Nat. Sci. Mater. 22 (2012) 644–653.
[36] X. Zou, C. Ran, Y. Dong, Z. Chen, D. Dong, D. Hu, X. Li, Y. Cui, RSC Adv. 6 (2016) 20664–20670.
[37] J. Wang, J. Li, H. Li, S. Duan, S. Meng, X. Fu, S. Chen, Chem. Eng. J. 330 (2017) 433–441.
[38] A.I. Becerro, J. Criado, L.C. Gontard, S. Obregón, A. Fernández, G. Colón, M. Ocaña, Cryst. Growth Des. 14 (2014) 3319–3326.
[39] Y. Zhu, Q. Ling, Y. Liu, H. Wang, Y. Zhu, Appl. Catal. B Environ. 187 (2016) 204–211.
[40] C. Pan, J. Xu, Y. Chen, Y. Zhu, Appl. Catal. B Environ. 115–116 (2012) 314–319.
[41] Y.H. Lv, Y.F. Liu, Y.Y. Zhu, Y.F. Zhu, J. Mater. Chem. A 2 (2014) 1174–1182.
[42] Y. Lv, Y. Zhu, Y. Zhu, J. Phys. Chem. C 117 (2013) 18520–18528.
[43] Z. Wu, J. Liu, Q. Tian, W. Wu, ACS Sustain. Chem. Eng. 5 (2017) 5008–5017.
[44] J. Geng, W.-H. Hou, Y.-N. Lv, J.-J. Zhu, H.-Y. Chen, Inorg. Chem. 44 (2005) 8503–8509.
[45] F. Xue, H. Li, Y. Zhu, S. Xiong, X. Zhang, T. Wang, X. Liang, Y. Qian, J. Solid State Chem. 182 (2009) 1396–1400.
[46] M. Guan, J. Sun, F. Tao, Z. Xu, Cryst. Growth Des. 8 (2008) 2694–2697.
[47] Q. Zhang, H. Tian, N. Li, M. Chen, F. Teng, CrystEngComm 16 (2014) 8334–8339.
[48] H. Yu, T. Cui, Z. Liu, J. Energy Chem. 25 (2016) 621–626.
[49] J. Wang, H. Li, S. Meng, L. Zhang, X. Fu, S. Chen, Appl. Catal. B Environ. 200 (2017) 19–30.
[50] D.J. Martin, K. Qiu, S.A. Shevlin, A.D. Handoko, X. Chen, Z. Guo, J. Tang, Angew. Chem. Int. Ed. 53 (2014) 9240–9245.
[51] L. Zhang, X. Fu, S. Meng, X. Jiang, J. Wang, S. Chen, J. Mater. Chem. A 3 (2015) 23732–23742.
[52] S. Liu, M.-Q. Yang, Y.-J. Xu, J. Mater. Chem. A 2 (2014) 430.
[53] P.X. Wang, J.J. Xian, J. Chen, Y.H. He, J.X. Wang, W.J. Li, Y. Shao, D.Z. Li, Appl. Catal. B-Environ. 144 (2014) 644–653.
[54] M. Zhao, G. Li, L. Li, L. Yang, J. Zheng, Cryst. Growth Des. 12 (2012) 3983–3991.
[55] Y. Zhu, Y. Liu, Y. Lv, Q. Ling, D. Liu, Y. Zhu, J. Mater. Chem. A 2 (2014) 13041–13048.
[56] L. She, G. Tan, H. Ren, C. Xu, C. Zhao, A. Xia, J. Alloys. Compd. 662 (2016) 220–231.
[57] B. Romero, S. Bruque, M.A.G. Aranda, J.E. Iglesias, Inorg. Chem. 33 (1994) 1869–1874.
[58] C. Fu, G. Li, M. Zhao, L. Yang, J. Zheng, L. Li, Inorg. Chem. 51 (2012) 5869–5880.
[59] Y. Zhang, M. Sillanpää, S. Obregón, G. Colón, J. Mol. Catal. A Chem. 402 (2015) 92–99.
[60] M. Zhao, L. Li, L. Yang, J. Zheng, G. Li, CrystEngComm 15 (2013) 609–615.
[61] B.S. Naidu, B. Vishwanadh, V. Sudarsan, R.K. Vatsa, Dalton Transactions 41 (2012) 3194–3203.
[62] M. Zhao, G. Li, J. Zheng, L. Li, H. Wang, L. Yang, CrystEngComm 13 (2011) 6251–6257.
[63] Z. Wei, Y. Liu, J. Wang, R. Zong, W. Yao, J. Wang, Y. Zhu, Nanoscale 7 (2015) 13943–13950.
[64] J. Tauc, R. Grigorovici, A. Vancu, Phys. Status Solidi B 15 (1966) 627–637.
[65] J. Meng, Q. Lin, T. Chen, X. Wei, J. Li, Z. Zhang, Nanoscale 10 (2018) 2908–2915.
[66] F. Tian, H. Zhao, G. Li, Z. Dai, Y. Liu, R. Chen, ChemSusChem 9 (2016) 1579–1585.
[67] P. Zhao, Y.L. Li, L.L. Li, S.L. Bu, W.L. Fan, J. Phys. Chem. C 122 (2018) 10737–10748.
[68] J. Xu, L. Li, C.S. Guo, Y. Zhang, W. Meng, Appl. Catal. B-Environ. 130 (2013) 285–292.
[69] Y. Guo, P. Wang, J. Qian, Y. Ao, C. Wang, J. Hou, Appl. Catal. B Environ. 234 (2018) 90–99.
[70] X. Fu, D. Huang, Y. Qin, L. Li, X. Jiang, S. Chen, Appl. Catal. B Environ. 148–149 (2014) 532–542.
[71] J. Li, Y. Wang, Y. Tian, X. He, P. Yang, M. Yuan, Y. Cao, J. Lyu, Environ. Sci. Pollut. Res. Int. 25 (2018) 15662–15670.
[72] W.Y. Zhou, J.Y. Liu, J.Y. Song, J.J. Li, J.H. Liu, X.J. Huang, Anal. Chem. 89 (2017) 3386–3394.
[73] V. Brezova, P. Tarabek, D. Dvoranova, A. Stasko, S. Biskupic, J. Photochem. Photobiol. A Chem. 155 (2003) 179–198.
[74] F. Chen, Y. Xie, J. He, J. Zhao, J. Photochem. Photobiol. A Chem. 138 (2001) 139–146.
[75] Y. Li, B. Wen, C. Yu, C. Chen, H. Ji, W. Ma, J. Zhao, Chem Eir. J. 18 (2012) 2030–2039.
[76] Y. Liu, Y. Zhu, J. Xu, X. Bai, R. Zong, Y. Zhu, Appl. Catal. B Environ. 142–143 (2013) 561–567.
[77] K. Ogisu, A. Ishikawa, Y. Shimodaira, T. Takata, H. Kobayashi, K. Domen, J. Phys. Chem. C 112 (2008) 11978–11984.

5850–5855.